Nano-size boron carbide intercalated graphene as high performance catalyst supports and electrodes for PEM fuel cells

Shichun Mu[*], Xu Chen, Ronghui Sun, Xiaobo Liu, Hui Wu, Daping He, Kun Cheng

State Key Laboratory of Advanced Technology for Materials Synthesis and Processing, Wuhan University of Technology, 430070, China

A R T I C L E   I N F O

A B S T R A C T

The low utilization and stability of noble-metal catalysts is always a big barrier to commercialize proton exchange membrane (PEM) fuel cells. Here we report a positive progress on stabilizing the catalyst by modulating 2D graphene as an advanced support of Pt nanoparticles, where the interlayer of graphene is near perfectly intercalated by nano-B_4C ceramics. The strong restriction effect of nano-ceramics in graphene interlayers, can greatly improves the usage and electrochemical stability of Pt catalysts. As results, our new graphene/B_4C supported Pt catalyst (Pt-RGO/B_4C) shows greatly enhanced electro-chemical surface area (121 m^2 g^{-1}) and mass activity (185 A g^{-1} Pt) towards oxygen reduction reaction (ORR), which is remarkably higher than the reduced graphene oxide (RGO) supported Pt (Pt/RGO) catalyst and the commercial Pt/C catalyst. In addition, the Pt-RGO/B_4C electrode also possesses higher fuel cell performance than the Pt/RGO electrode. Especially, after the electrochemical acceleration test for 10000 cycles, our new catalyst presents an excellent stability, even retains 45.2% initial electrochemical surface area, while the Pt/RGO and Pt/C are only 29.7 and 23.4%, respectively. These indicate our unique catalyst is promising to allow the PEM fuel cell have high ORR activity and stability.

© 2016 Elsevier Ltd. All rights reserved.

1. Introduction

Direct-hydrogen-fueled proton exchange membrane (PEM) fuel cells are promising to address the serious energy and environmental crises to human beings due to their high efficiency and eco-friendly product (water). Thus they are promising to be widely used as the vehicle, portable and stationary power systems [1] as well as the storage system for solar and wind energy [2,3]. However, the lower electrochemical stability of Pt based catalysts predominantly caused by the degradation of electrochemical specific surface area (ECA) of metallic Pt radically hinders the commercialization of PEM fuel cells [4–6]. The ECA loss of Pt could be derived from the dissolution at high potentials, and the aggregation of Pt nanoparticles (NPs) caused by the Ostwald ripening of Pt species, motion or detachment of Pt NPs on/from supports [7,8]. Among them, the motion and detachment of Pt NPs could be controllable in terms of improving the interaction between metal-support and employing the oxidation-resisted supports.

At present, the common used catalyst support is nanocarbon

black of 40–50 nm size in diameter with good conductivity and rich micropores (e.g., valcan XC-72) which benefit the dispersion of Pt NPs [9]. However, some Pt NPs would be fallen into micropores grown in surfaces of nanocarbon black and lead to the low Pt usage due to the inaccessibility to electrolytes, which increases the loss of the triple phase boundary [10]. Moreover, it easily suffers from oxidation, resulting in the detachment and aggregation of Pt NPs [11]. These bring about the critical ECA decay of Pt catalysts. Graphitic carbon such as carbon nanotubes, graphene is attracted as the durable supports. Among them, graphene as a unique 2D material endows its excellent physical properties including high theoretical surface area of over 2000 m^2/g, electrical conductivity and mechanical stability as well as good chemical stability, which is a promising support material to replace conventional nanocarbon black [12–15]. However, its strong chemically inert and hydrophobic surfaces trigger the poor interaction between metal-support, leading to the aggregation of Pt NPs [16]. Thus graphene oxide (GO), with affinity surfaces, is often employed as the advanced support [17,18]. But unfortunately, the structure and morphology of GO nanosheets are not stable, they are readily curled, restacked or wrinkled [19–21], greatly decreasing the geometry surface area. At the same time, Pt NPs would be covered or wrapped by the

---

deformed nanosheet, which reduces the triple phase boundary on Pt and brings about the low usage and stability of Pt catalysts.

To confine the deformation of GO nanosheets, recently, GO/nano-pilar (e.g., nanocarbon, nanoceramics) intercalation composites have been developed [19–22]. Herein, the graphene layer can be separated and blocked by conductive nanopilars, and thus 2D GO nanosheets can be effectively remained. As carbon building blocks, nanocarbon is prone to electrochemical oxidation because carbon belongs to an unstable thermodynamic matter. In contrast, most of the nanoceramics (e.g., ZrC, ZrB$_2$, SiC, B$_4$C, TiO$_2$) have very excellent chemical and electrochemical stability either in acid or alkaline media, and comparable electrical conductivity to carbon [9,23–25]. As expected, the prepared GO/nano-ceramics supported Pt catalyst could show high ECA value and superior stability than the pristine GO supported Pt and commercial Pt/C catalysts. However, as we know, the specific weight (SW) of graphene (~1.0) [26], GO (~2.2) [27] and reduced GO (RGO) (~1.0 < SW<~2.2) is significantly lower than the common ceramics (e.g., ~3.0 for SiC), which would increase the resistance of insertion of nanoceramics into graphene interlayers. This means the satisfying grapehene intercalation composite cannot be obtained by simply blending the light graphene with the heavy nanocermaics.

In this work, a new and lighter nanoceramic, B$_4$C (SW is ~2.5), is applied to match the SW of graphene. Moreover, differently from the conventional method, prior to mixing the graphene and ceramics, the SW of graphene is modulated by depositing Pt NPs on graphene nanosheets in advance. This special step can further balance the SW between the nanoceramic and graphene, which benefits the acquirement of the almost perfect nanoceramic intercalated graphene composite. At the same time, B$_4$C nanoceramics also can be as the conducting media between graphene due to its good electron conductivity comparable to the commercial conductive carbon black (e.g., vulcan XC 72 carbon) [25]. As results,

the platinized intercalation architecture presents very high electrochemical activity area and outstanding stability.

2. Experimental

2.1. Preparation of the Pt-RGO/B$_4$C catalyst

Graphene oxide (GO) was fabricated by exfoliating the natural graphite using the modified hummer method [28], and then added into the ethylene glycol solution (81 mg of GO). After ultrasonicated for 1 h, the highly dispersed GO suspension solution can be obtained and then moved into a 500 ml round bottom flask. Subsequently, H$_2$PtCl$_6 \cdot$6H$_2$O (7 mL, 1 mg mL^{-1} Pt) and ethylene glycol (100 mL) mixed solution was added dropwise into the GO suspension and stirred vigorously for 20 min at room temperature. The value of the solution pH was adjusted to 8–10 making use of 1.0 M NaOH solution, followed by the heat-treatment under reflux at 130 °C for 1–2 h until the color of the solution changed from buff to black, which indicated the Pt precursor was completely reduced into nanoparticles (NPs) and simultaneously the reduced GO (RGO) appeared. After that, 10 mg of nano B$_4$C solid powders with 50 nm average particle size was homogeneously dispersed into the ethylene glycol solution, and then was blended with the Pt/RGO suspension and stirred overnight. After filtered, washed with deionized water for three times, and dried in a vacuum oven at 80 °C for 8 h, the Pt-RGO/B$_4$C catalyst was obtained. As benchmarks, RGO supported Pt catalysts (Pt/RGO) were prepared following the same process and the commercial 20 wt.% Pt/C catalyst bought from Johnson Matthey was applied.

2.2. Structural characteristics

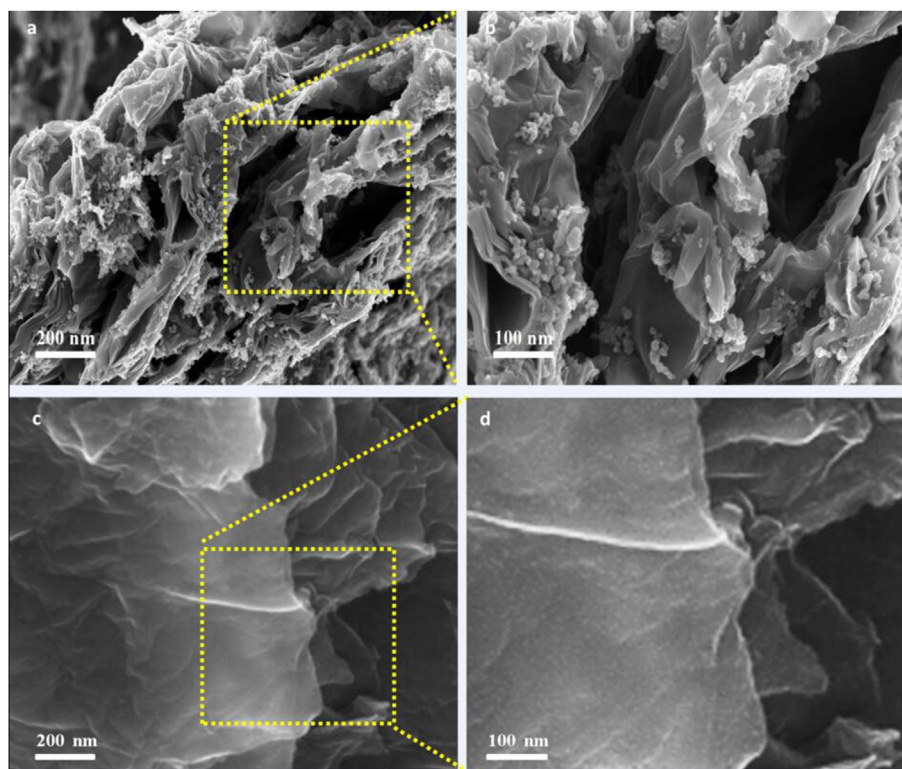The morphology and structure of the catalysts were investigated

Fig. 1. SEM images of Pt-RGO/B$_4$C (a) and Pt/RGO (c) catalysts, and corresponding magnification ones for the former (b) and the latter (d). (A color version of this figure can be viewed online.)
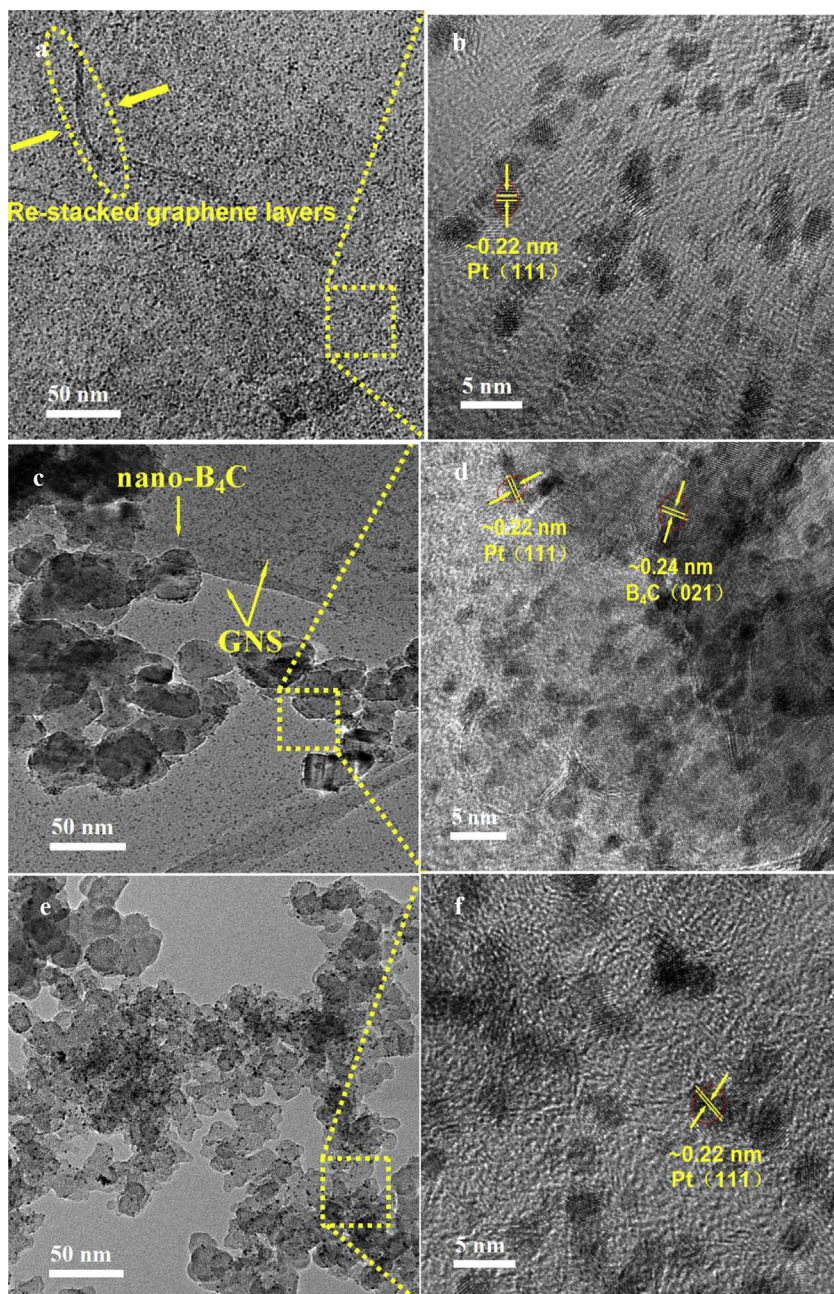
Fig. 2. TEM images of Pt/RGO (a), Pt-RGO/B$_4$C (c) and Pt/C (e) catalysts, and corresponding magnification ones for Pt/RGO (b), Pt-RGO/B$_4$C (d) and Pt/C (f). (A color version of this figure can be viewed online.)

using JEOL JEM 6700 scanning electron microscope (SEM) operated at 10 kV, JEOL 2010 high-resolution transmission electron microscope (HRTEM), and X-ray diffraction with Cu K$_\alpha$ source ($\lambda = 1.54056$ Å) at a scan rate of 5° min^{-1} from 10 to 80°. Raman spectroscopy was performed on a Renishaw using Ar ion laser with an excitation wavelength of 514.5 nm.

2.3. Electrochemical characteristics

Electrochemical measures were performed at (298 ± 1) K in a 3-electrode half-cell configuration, using an Autolab PGSTAT30 potentiostat (EcoChemie B.V, Holland) and a RDE setup (Pine Instruments). The electrolyte was 0.1 M double distilled ultrapure perchloric acid (HClO$_4$) diluted from 70% (Sinopharm Chemical

Reagent Co., Ltd). A platinum wire and a saturated calomel electrode were used as a counter electrode and a reference electrode, respectively. Herein, all the potentials were referenced to the reversible hydrogen electrode (RHE).

To prepare the catalyst ink, 20 wt.% Pt-containing catalyst (3 mg) was blended with 480 uL ultrapure water (R = 18.2 MΩ), 20 uL 5 wt.% Nafion (DuPont Co., Ltd.) solution and 500 uL isopropanol, and then ultrasonicated for 0.5 h in an ultrasonic bath (Grant Instruments, 38 kHz). The working electrode was made by dropping catalytic ink (5 μ) onto a glassy carbon disk (d = 5.0 mm), the total Pt loading was approximately 15 μgPt cm^{-2}. Then the solvent was removed under a N$_2$ stream at room temperature.

To measure the electrochemical specific surface area (ECA), the HClO$_4$ solution was bubbled with N$_2$ for 20 min, and then the
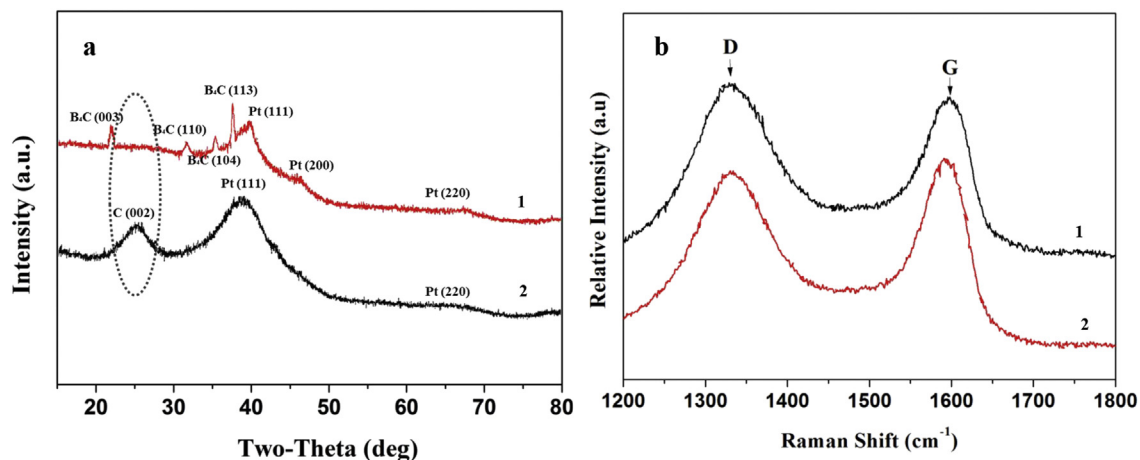
Fig. 3. XRD patterns (a) and Raman spectra (b) of Pt-RGO/B₄C and Pt/RGO catalysts. (1) Pt-RGO/B₄C, (2) Pt/RGO. (A color version of this figure can be viewed online.)

electrode was conditioned by potential cycling under N_2 for 50 cycles (from 0 to +1.2 V vs. RHE) at 100 mV s^{-1}. Cyclic voltammograms (CVs) were recorded under N_2 in a 1 M HClO$_4$ solution at a scan rate of 50 mV s^{-1} with a potential window of 0 to +1.2 V vs. RHE at room temperature. After that, Linear scan voltammogram (LSV) was carried out to investigate oxygen reduction reaction (ORR) of catalysts using a rotating disk electrode in 0.1 M HClO$_4$ at a sweep rate of 10 mV s^{-1} and a speed of 1600 rpm at room temperature. To evaluate the stability of catalysts, an electrochemically accelerated durability test (ADT) was undertaken by continuous CVs between +0.6 and + 1.2 V vs. RHE. After certain cycles of potential scan, CV curves were carried out from 0 to +1.2 V vs. RHE at a scan rate of 50 mV s^{-1}.

2.4. Fuel cell performance characteristics

Single cell tests were carried out to examine the fuel cell performance using the prepared catalysts. Prior to testing, catalyst coated membranes (CCMs) were fabricated by a decal method [29,30]: Firstly, the Pt/C catalyst (20 wt.%, Johnson Matthey) was dispersed in a mixture of 5 wt.% Nafion® solution (Du Pont), deionized water and isopropyl alcohol by ultrasonication for 20 min; Then the obtained catalyst ink was sprayed on Teflon sheets and dried at 100 °C for 1 h; After that, the formed catalyst layers was transferred on both sides of the Nafion® NRE 211 membrane (Du Pont) by subsequent hot-pressing for 2 min at 2 MPa and 160 °C. Single cells were assembled by integrating as-prepared CCMs, gaskets, gas diffusion layers with porous layers (WUT Energy Co.), graphite bipolar plates with straight flow field channels, and copper end plates with gold-plating. The active area of CCMs was 5 cm^{-1} × 5 cm^{-1} with the Pt loading of 0.08/0.11 mg cm^{-2} at corresponding anode/cathode sides. Single cell tests were completed using G50 Fuel Cell Test Station (GreenLight) under H$_2$/Air (1.5/1.8 stoic), a back pressure of 150 kPa and a temperature of 70 °C. The humidity was 80 and 100% RH at corresponding anode/cathode sides.
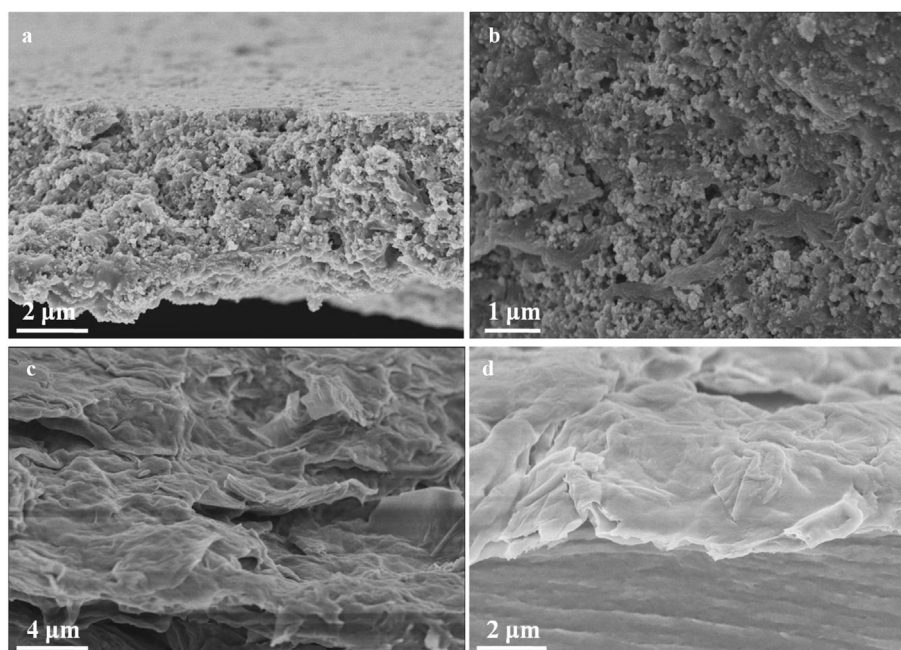

Fig. 4. SEM cross-sections of Pt-RGO/B₄C (a, b) and Pt/RGO (c, d) catalyst layers.
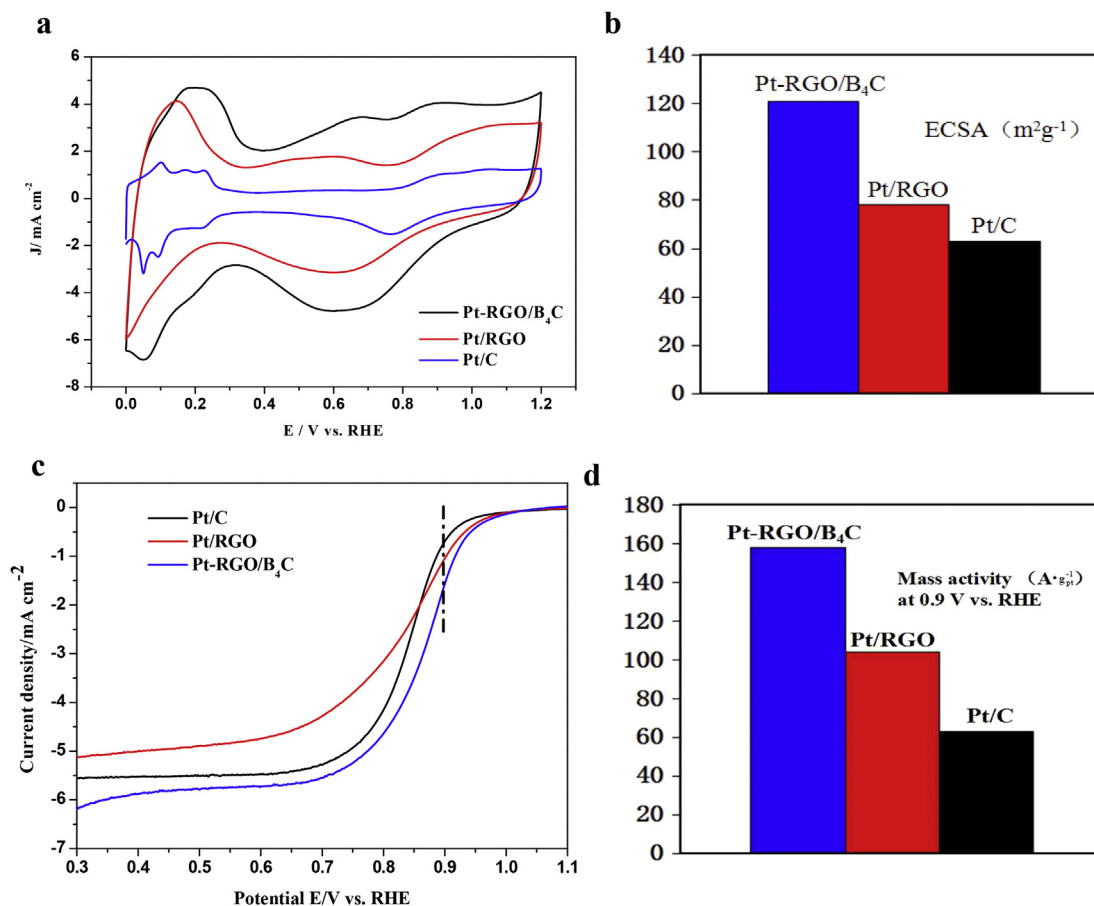
Fig. 5. CV curves (a) and ECA (b) of Pt-RGO/B₄C, Pt/RGO and commercial Pt/C catalysts; LSV polarization curves for ORR (c) and mass activities at +0.9 V vs. RHE (d) in 0.1 M HClO₄ solution. (A color version of this figure can be viewed online.)

3. Results and discussion

Morphologies of the Pt-RGO/B₄C and Pt/RGO catalysts were investigated by SEM observations. As shown in Fig. 1a and b, graphene nanosheets are almost fully exfoliated by inserting nano-B₄C ceramics, and the typical sandwich-like layered structural of graphene is well remained even the interlamellar spacing of the intercalation greatly increases. As pillars, the insertion of nano-B₄C NPs into graphehe interlayers blocks the π—π bonding of graphehe nanosheets, avoiding the radical structural deformation of nanosheets under the harsh operating condition. Moreover, the expanded spacing can facilitate the exposure of more Pt NPs on both sides of graphene to the electrolyte, enhancing the ECA by increasing the triple phase boundary on Pt surfaces, and simultaneously speed up the mass transfer for reaction species by increasing the amount of pathways and shortening the transfer distance. These are beneficial to improve the catalytic activity and the output power at large current densities. In contrast, the obvious restacking and crumpled structures of graphene occur in Pt/RGO (Fig. 1c and d) due to the strong π—π bonding between nanosheets, especially at their edges, indicating the intrinsical instability of 2D nanosheets. Understandably, some Pt NPs would be encapsulated by graphene, leading to low usage of Pt and poor mass transfer for electrodes.

The structure of the Pt-RGO/B₄C and Pt/RGO catalysts was further probed using the TEM technique. Fig. 2a and b shows highly dispersed Pt NPs, with average size of 2.6 nm in diameter, are homogeneously deposited on RGO. This is because GO has abundant oxygen-containing groups which is beneficial for adsorbing Pt species due to the strong affinity between them [18]. After the reduction reaction, most of Pt NPs then evenly attached onto RGO surfaces. The lattice fringes with spacing d = 0.22 nm are ascribe to Pt (111) facets (Fig. 2b). However, restacking or folding structures can be observed, which would cover or encapsulate some Pt NPs and lead to the low efficient usage of Pt. This is in good agreement with the results of the SEM observation as shown in Fig. 1c and d. Similarly to the case of Pt/RGO, for Pt-RGO/B₄C (Fig. 2c), it can be seen that Pt NPs, with average size of 2.5 nm in diameter, are also highly dispersed on RGO. As shown in Fig. 2d, the lattice fringes of 0.22 and 0.24 nm in the spacing are assigned to Pt (111) and B₄C (021) facets, respectively. The average size of B₄C is approximately 50 nm. However, differently from Pt/RGO, almost all graphene nanosheets remain flat due to the blocking effect of B₄C nano-ceramic intercalation, which can maintain the full exposure of Pt NP to electrolytes, improving the Pt availability to electrocatalysis. As another benchmark, the TEM image of the commercial Pt/C is shown in Fig. 2e and f, Pt NPs with average size of 2.8 nm are also uniformly deposited on sphere-like nanocarbon black (40—50 nm in diameter).

Fig. 3a reveals XRD patterns of Pt-RGO/B₄C and Pt/RGO. A broad hump at a 2θ value of 23—25° for Pt/RGO can be attributed to the feature (002) diffraction peak of graphene nanosheets derived from the graphite crystal [31]. However, the (002) peak of graphene cannot be observed in the same range (the circled region with a dash line) for Pt-RGO/B₄C, suggesting that graphene nanosheets are ideally exfoliated due to the favorable insertion of nano-B₄C into
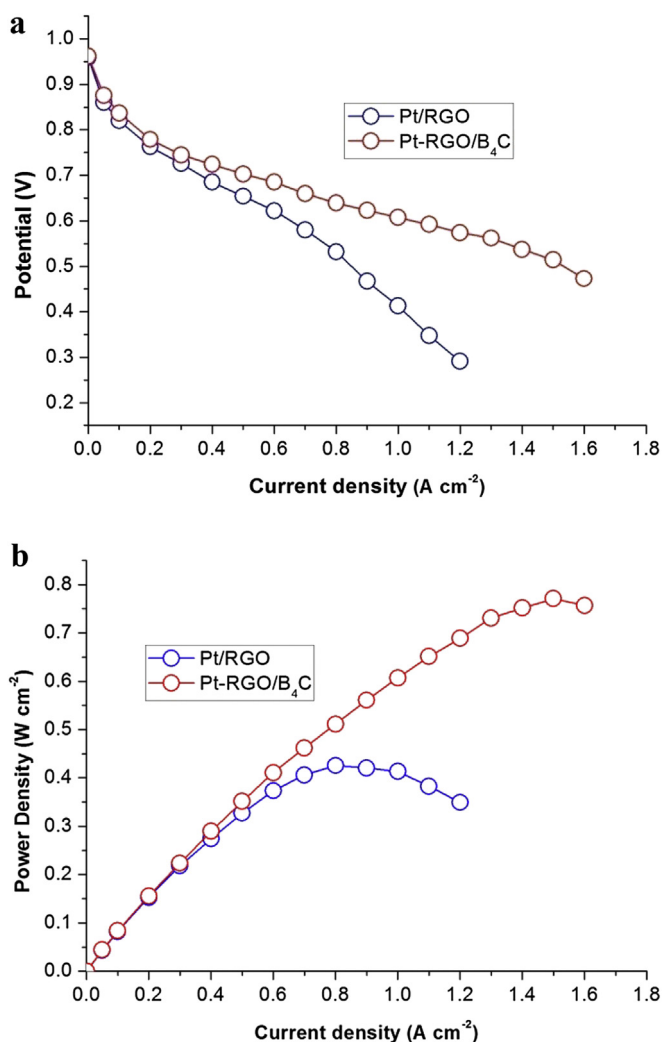
Fig. 6. Fuel cell polarization curves obtained by single cell tests (a) and power density (b) for Pt-RGO/B$_4$C and Pt/RGO electrodes. (A color version of this figure can be viewed online.)

interlayers of graphene. To further probe the structure of Pt-RGO/B$_4$C, Raman spectra were performed. Fig. 3b shows two distinguished peaks at 1348 and 1585 cm^{-1}, which are attributed to D and G bands, respectively. Usually, D and G bands correspond to the disordered carbon and the graphitic carbon (or ordered carbon), respectively [32]. Thus, the ratio of the intensity of D band to G
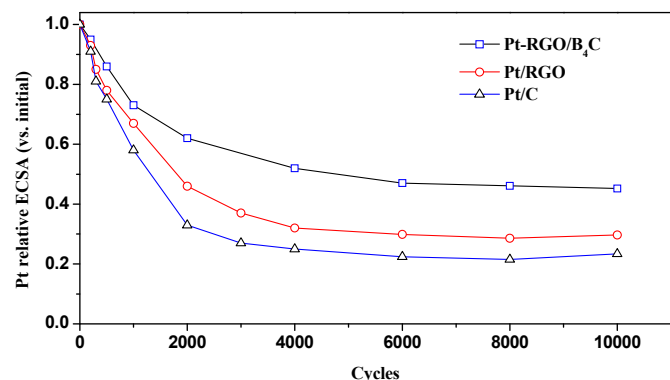

Fig. 7. ECSA decay as a function of the number of potential cycles. (A color version of this figure can be viewed online.)

band is often applied to evaluate the graphitization degree or disorder for carbon materials. For Pt-RGO/B$_4$C and Pt/RGO samples, their values correspond to 1.01 and 0.94, revealing that, from Pt/RGO to Pt-RGO/B$_4$C, the degree of disorder for graphene increases. This is because the introduction of B$_4$C intercalation greatly enlarges the spacing of graphene, leading to the well-done exfoliation of graphene. This structural property is consistent with the investigation results using SEM/TEM and XRD techniques, indicating our assumption that platinizing GNS could promote the insertion of nano-ceramics into GNS by balancing the SW between GNS and ceramics is logical.

The microstructure of the catalyst layer was also analyzed by collecting the dried filter cake of the catalysts. Fig. 4a shows a loose and porous catalyst layer consists of the platinized RGO and the B$_4$C intercalation. When further magnifying the catalyst layer, the porous B$_4$C intercalated RGO composite structure is visible (Fig. 4b), which is consistent with the observed result from SEM (Fig. 1a and b). This demonstrates the intercalation structure can be well preserved in the catalyst layer, which would facilitate the improvement of activity and stability of Pt catalysts. In contrast, as shown in Fig. 4c and d, a compact layer-by-layer restacking structure can be found, which is in good agreement with the result of SEM (Fig. 1c and d). This decreases the Pt utilization and is unavailable to mass transfer.

The CV curves of the catalysts were recorded in a 0.1 M HClO$_4$ electrolyte solution to calculate their ECA values according to the hydrogen desorption area at 0-+0.25 V vs. RHE (Fig. 5a and b) [33]. ECA reflects the available active site on Pt surfaces in electrochemical environments. As can be seen in Fig. 5b, the ECA value of Pt-RGO/B$_4$C is up to 121 m^2 g^{-1}, which is greatly larger than that of Pt/RGO (78 m^2 g^{-1}) and Pt/C (63 m^2 g^{-1}), respectively. Also it outperforms the B$_4$C nanoceramic supported Pt catalyst (20 wt.% Pt/B$_4$C, ~88 m^2 g^{-1} in H$_2$SO$_4$ media) [25]. This indicates Pt-RGO/B$_4$C has high utilization of Pt catalysts. The width of the CV curve at 0.3−0.8 V represents the electric double layer capacitor (EDLC), which can be used to assess the geometry surface area of materials, especially the accessibility of the geometry surface area to the electrolyte. It can be seen that the EDLC of Pt-RGO/B$_4$C and Pt/RGO is greater than Pt/C, indicating graphene possesses higher available surface area than carbon black. In contrast, to compare Pt/RGO, the EDLC of Pt-RGO/B$_4$C is higher, further proving that its high accessibility of the surface area to the electrolyte due to the stabilized graphene structure in Pt-RGO/B$_4$C with enlarged interlayer spacing, as shown in Fig. 1.

The polarization curves of the half cell for catalysts were given through LSV in oxygen-saturated 0.1 M HClO$_4$ with at 1600 rpm (Fig. 5a and b). As shown in Fig. 5a, Pt-RGO/B$_4$C exhibits higher initial potential and half-wave potential than both Pt/RGO and Pt/C, indicating Pt-RGO/B$_4$C has the highest ORR performance among catalysts. The kinetic current (i_k) was calculated by the Koutecky-Levich equation [34]. Then the ORR mass activity for catalysts was obtained using i_k divided by the Pt loading at 0.9 V vs. RDE. As shown in Fig. 5b, the mass activity of Pt-RGO/B4C is 185 A g^{-1}, which is 1.8 and 2.9 times higher than that of Pt/RGO and Pt/C, respectively. The resultant can be attributed to higher usage of Pt NPs on the B$_4$C intercalated RGO nanocomposite, which is consistent with the CV result.

The fuel cell performance of the Pt-RGO/B$_4$C catalyst was investigated to reveal its applicability. Fig. 6 shows the polarization curves of single fuel cells with different catalysts, among them the cell with Pt-RGO/B$_4$C possesses the highest output voltage at all the current densities. The fast voltage drop at the low current is mainly caused by the sluggish ORR kinetics at the cathode. When elevating the current density, the differentia of output voltage varies considerably between Pt-RGO/B$_4$C and Pt/RGO electrodes,
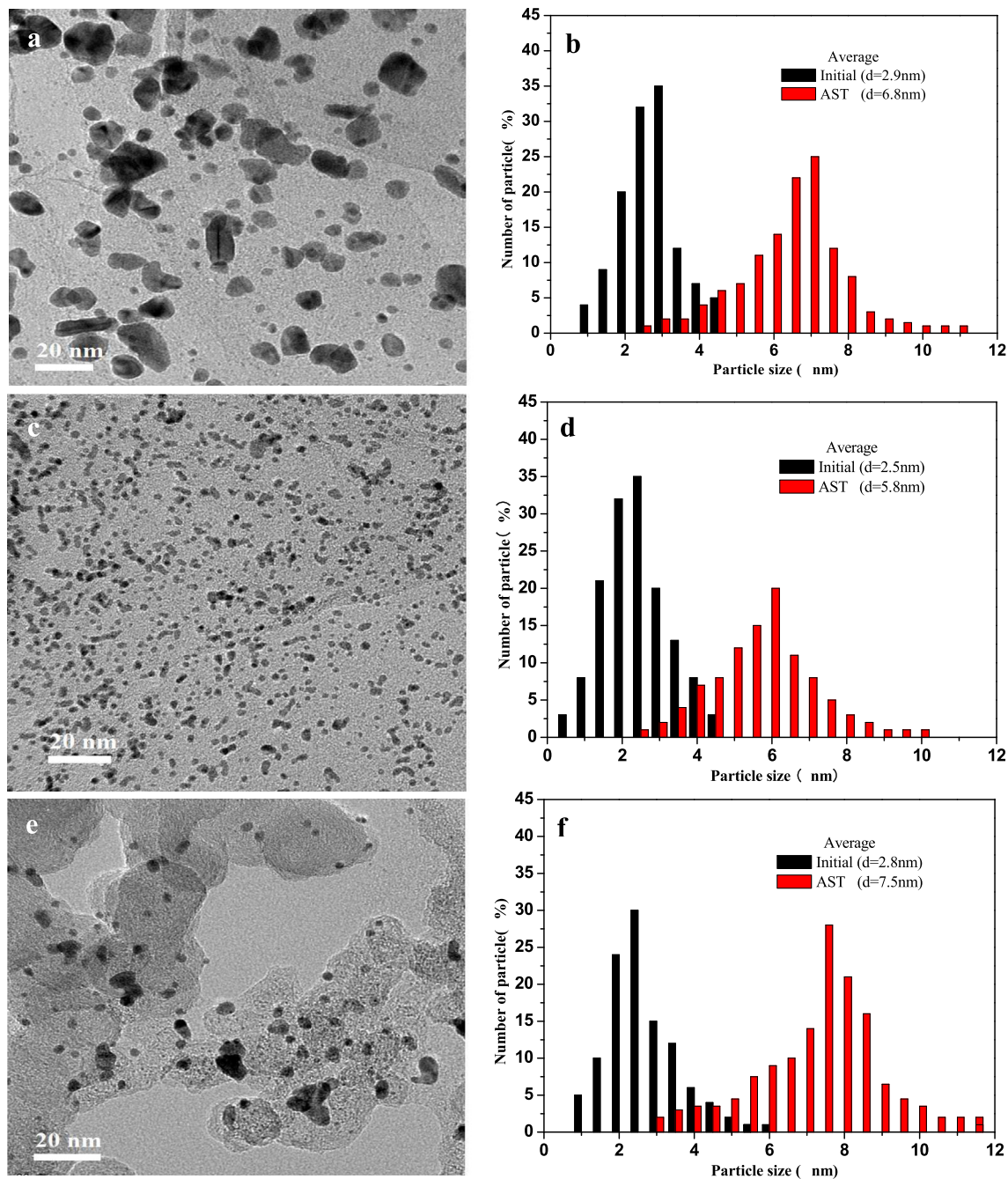
Fig. 8. TEM images of the Pt/RGO (a), Pt-RGO/B₄C (b) and Pt/C (c) catalysts after ADT, and corresponding Pt particle size distributions of Pt/RGO (d), Pt-RGO/B₄C (e) and Pt/C (f)before (black) and after (red) ADT. (A color version of this figure can be viewed online.)

especially at the larger current densities which are controlled by a diffusion step. At 1.0 A/cm^2 and low Pt loading of 0.19 mgPt/cm^2, the output voltage of the Pt-RGO/B₄C electrode is 0.607 V, which is greater than the Pt/RGO electrode (0.413 V). This voltage difference is up to 194 mV, indicating the Pt-RGO/B₄C electrode has superior mass transfer capability for reaction species than the PtRGO electrode. The maximum power density of the former reaches 771 mw/cm^2 (0.25 gPt/kW) which increases by 345 mw/cm^2 over the latter. The high fuel cell performance of Pt-RGO/B₄C can be ascribed to its unique B₄C intercalated graphene structure which allows Pt NPs own outstanding activity and mass transfer capability in comparison with Pt/RGO where some Pt NPs are veiled by the crumpled

graphene nanosheets and the mass transfer pathways are blocked by the compact layer-by-layer stacking structure of graphene.

The electrochemically accelerated durability test (ADT) was carried out to characterize the stability of catalysts. Fig. 7 shows all ECA values decay with the increased cycle number. This is due to the inevitable dissolution and dissolution-reprecipitation of Pt NPs, and the aggregation and detachment of crystalline Pt under harsh electrochemical conditions, which leads to the loss of active sites of Pt. In contrast, to compare with Pt/RGO and Pt/C, Pt-RGO/B₄C has low loss rate of ECA during ADT. Even after 10000 potential cycles, 45.2% of the initial ECA remains, while it is only 29.7% and 23.4% for Pt/RGO and Pt/C, respectively. This can be further evidenced by the

morphology analysis of Pt NPs from TEM images after ADT. As seen in Fig. 8a, c and e, to compare with the pristine Pt NPs, the enlarged size and decreased number of Pt NPs can be found to varying degree after 10000 potential cycles for all samples, leading to the ECA loss of Pt catalysts. However, for Pt-RGO/B$_4$C, the increase of the Pt particle size (from 2.5 to 5.8) nm is sluggish (Fig. 8b) in comparison with that of Pt/RGO from 2.6 to 6.8 nm (Fig. 8d) and Pt/C from 2.8 to 7.5 nm (Fig. 8f). Also, for Pt-RGO/B$_4$C the reduction of the Pt particle number is limited (Fig. 8c), while it is visible for Pt/RGO (Fig. 8a) and Pt/C (Fig. 8e). The outstanding stability of Pt-RGO/B$_4$C can be attributed to its higher structural stability than that of Pt/RGO and to the superior oxidation-resistant of graphene supports than carbon black for Pt/C. Moreover, the presence of B$_4$C blocks could hinder the motion of Pt NPs on RGO. As results, the aggregation and detachment of Pt NPs are effectively prohibited.

4. Conclusions

The near perfect nano-ceramic intercalated graphene structure was prepared by selecting the lower specific weight nano-B$_4$C as the intercalation to match the graphene. Thus the 2D graphene structure can be maintained well under electrochemical operating environments. As supporting Pt NPs, the novel catalyst shows prominent electrochemical active surface area, mass activity and mass transfer capability over the pristine graphene supported Pt catalyst (Pt/RGO) and the commercial Pt/C catalyst. At the same time, using our catalyst as the electrode, the fuel cell performance is better than that of the Pt/RGO electrode. Significantly, this catalyst also exhibited higher stability than Pt/RGO and Pt/C. The greatly improved electrochemical properties of our novel catalyst can be attributed to the presence of B$_4$C intercalations between graphene layers that stabilize the 2D graphene structure and enlarge graphene interlayer spacing, enhancing the usage of Pt and shortening the transfer pathway of reaction species as well as prohibit the motion, aggregation and detachment of Pt NPs on graphene.

References

[1] Y. Wang, K.S. Chen, J. Mishler, S.C. Cho, X.C. Adroher, Appl. Energy 88 (2011) 981—1007.
[2] D. Rekioua, S. Bensmail, N. Bettar, Int. J. Hydrogen Energy 39 (2014) 1604—1611.
[3] M. Eroglu, E. Dursun, S. Sevencan, J. Song, S. Yazici, O. Kilic, Int. J. Hydrogen Energy 36 (2011) 7985—7992.
[4] M.K. Debe, Nature 486 (2012) 43—51.
[5] Y. Zhang, S. Chen, Y. Wang, W. Ding, R. Wu, L. Li, X.Q. Qi, Z.D. Wei, J. Power Sources 273 (2015) 62—69.
[6] N. Cheng, M.N. Banis, J. Liu, et al., Adv. Mater. 27 (2015) 277—281.
[7] J. Ying, X.Y. Yang, Z.Y. Hu, S.C. Mu, C. Janiak, W. Geng, M. Pan, X.X. Ke, G.V. Tendeloo, B.L. Su, Nano Energy 8 (2014) 214—222.
[8] K. Cheng, Z.K. Kou, J. Zhang, M. Jiang, H. Wu, L. Hu, X.Y. Yang, M. Pan, S.C. Mu, J. Mater. Chem. A 3 (2015) 14007—14014.
[9] H.F. Lv, S.C. Mu, Nanoscale 6 (2014) 5063—5074.
[10] N.C. Cheng, S.C. Mu, X.J. Chen, H.F. Lv, M. Pan, P.P. Edwards, Electrochim. Acta 56 (2011) 2154—2215.
[11] K. Cheng, Z.K. Kou, J. Zhang, M. Jiang, H. Wu, L. Hu, X.Y. Yang, M. Pan, S.C. Mu, J. Mater. Chem. A 3 (2015) 14007—14014.
[12] H.G. Li, N.C. Cheng, Y. Zheng, X. Zhang, H.F. Lv, D.P. He, M. Pan, F. Kleitz, S.Z. Qiao, S.C. Mu, Adv. Energy Mater 3 (2013) 1176—1179.
[13] X.J. Zhou, J.L. Qiao, L. Yang, J.J. Zhang, Adv. Energy Mater 4 (2014) 1301523.
[14] A. Marinkas, F. Arena, J. Mitzel, G.M. Prinz, A. Heinzel, V. Peinecke, H. Natter, Carbon 58 (2013) 139—150.
[15] D.P. He, K. Cheng, Y.L. Xiong, Z.K. Kou, X. Chen, M. Pan, S.C. Mu, Carbon 66 (2014) 312—319.
[16] D.P. He, S.C. Mu, M. Pan, Carbon 49 (2011) 82—88.
[17] M. Liu, R. Zhang, W. Chen, Chem. Rev. 114 (2014) 5117—5160.
[18] D.P. He, K. Cheng, T. Peng, X.L.L. Sun, M. Pan, S.C. Mu, J. Mater. Chem. A 22 (2012) 21298—21304.
[19] D.P. He, K. Cheng, T. Peng, M. Pan, S.C. Mu, J. Mater. Chem. A 1 (2013) 2126—2132.
[20] P. Wu, H.V. Lv, T. Peng, D.P. He, S.C. Mu, Sci. Rep. 4 (2014) 3968.
[21] X. Chen, D.P. He, H. Wu, X.F. Zhao, J. Zhang, K. Cheng, P. Wu, S.C. Mu, Sci. Rep. 5 (2015) 16246.
[22] Z.J. Fan, J. Yan, L.J. Zhi, Q. Zhang, T. Wei, J. Feng, M.L. Zhang, W.Z. Qian, F. Wei, Adv. Mater. 22 (2010) 3723—3728.
[23] N.C. Cheng, M.N. Banis, J. Liu, A. Riese, S.C. Mu, R.Y. Li, T.K. Sham, X.L. Sun, Energy Environ. Sci. 8 (2015) 1450—1455.
[24] S.Y. Huang, P. Ganesan, S. Park, B.N. Popov, J. Am. Chem. Soc. 131 (2009) 13898—13899.
[25] H.F. Lv, Niancai Cheng, Tao Peng, Mu Pan, Shichun Mu, High stability platinum electrocatalysts with zirconia-carbon hybrid supports, J. Mater. Chem. 22 (2012) 1135—1141.
[26] M.A. Rafiee, J. Rafiee, Z. Wang, H.H. Song, Z.Z. Yu, N. Koratkar, ACS Nano 3 (2009) 3884—3890.
[27] S. Stankovich, D.A. Dikin, G.H.B. Dommett, K.M. Kohlhaas, E.J. Zimney, E.A. Stach, R.D. Piner, S.T. Nguyen, R.S. Ruoff, Nature 442 (2006) 282—286.
[28] L.J. Cote, F. Kim, J.J. Huang, J. Am. Chem. Soc. 131 (2009) 11027—11032.
[29] S. Gottesfeld, M.J. Wilson, Appl. Electrochem. 22 (1) (1992) 355—363.
[30] S.C. Mu, P. Zhao, C. Xu, Y. Gao, M. Pan, Int. J. Hydrogen Energy 35 (2010) 8155—8160.
[31] J.B. Aladekomo, R.H. Bragg, Carbon 28 (1990) 897—906.
[32] S.C. Mu, H.L. Tang, S.H. Qian, M. Pan, R.Z. Yuan, Carbon 44 (2006) 762—767.
[33] M.J. Jiang, P.H.C. Camargo, E.C. Cho, J. Tao, X.M. Lu, Y.M. Zhu, Y.N. Xia, Science 324 (2009) 1302—1305.
[34] J. Masa, C. Batchelor-McAuley, W. Schuhmann, R.G. Compton, Nano Res. 7 (2014) 71—78.